Available online at https://link.springer.com/journal/42241
http://www.jhydrodynamics.com
Journal of Hydrodynamics, 2022, 34(2): 259-276
https://doi.org/10.1007/s42241-022-0029-0

Ship maneuvering prediction based on virtual captive model test and system dynamics approaches

Peng Du[1, 2, 3], Lu Cheng[2], Zi-jian Tang[2], A. Ouahsine[3], Hai-bao Hu[2*], Y. Hoarau[4]
1. *Research and Development Institute of Northwestern Polytechnical University in Shenzhen, Shenzhen 518057, China*
2. *School of Marine Science and Technology, Northwestern Polytechnical University, Xi'an 710072, China*
3. *Laboratoire Roberval, UT Compiègne-Sorbonne Université, Compiègne, France*
4. *ICUBE Laboratory, University of Strasbourg, Strasbourg, France*

(Received February 9, 2021, Revised August 22, 2021, Accepted November 1, 2021, Published online April 27, 2022)

Abstract: The maneuvering simulation is carried out through the continuous captive model test and the system dynamics approach. The mathematical maneuvering group (MMG) model is implemented in the virtual captive model tests by using the computational fluid dynamics (CFD) techniques. The oblique towing test (OTT), the circular motion test (CMT), the rudder force test and the open water test are performed to obtain the hydrodynamic derivatives of the hull, the rudder and the propeller, and the results are validated by experimental data. By designing the tests, the number of cases is reduced to a low level, to allow us to evaluate the maneuverability with a low cost and in a short time. Using these obtained coefficients, the system-based maneuvering simulations are conducted to calculate the position and the attitude of the ship, with results in agreement with the free running test results. This procedure can also be used for other hull forms, with reduced workload and with convenience for maneuvering simulation tasks.

Key words: Maneuvering simulation, captive model test (CMT), system dynamics, computational fluid dynamics (CFD), Hydrodynamic derivatives

Introduction

The ship maneuvering test is important for evaluating the maneuverability of a vessel, which involves the ability of the vessel to keep or change its motion state under the control actions, including the straight-line stability, the course-keeping ability, the course-changing ability, the yaw checking ability, the turning ability, and the stopping ability. Correspondingly, the turning circle test, the zig-zag test, the stopping test, the spiral test and the pull-out test might be carried out to determine these abilities. The standards of the ship maneuverability are formulated by the International Maritime Organization.

The methods and the procedures for the maneuvering tests were comprehensively reviewed in literature. These methods are classified as shown in Fig. 1. The maneuvering analysis can be performed either by the free running test or by the mathematical modeling (in full- or model-scale). The free running test is carried out for the functional propellers and rudders. The motion states are recorded and analyzed to characterize the maneuverability directly. Experimental data of ship maneuvering are very few, several studies were for the tankers, the DTMB 5415, the KVLCC1, the KVLCC2, the KCS, the ONRT, the SR108 by the Hamburgische Schiffbau-Versuchsanstalt GmbH (HSVA), the Ship Hydrodynamics Division, Centrum Techniki Okretowej (CTO), Poland, the Maritime Research Institute Nederlands (MARIN), the Schiffbau-Versuch- sanstalt Potsdam GmbH (SVAP), Germany, the Bulgarian Ship Hydrodynamic Center (BSHC), Bulgaria, the Ishikawajima Heavy Industries (IHI), Japan, the Iowa Institute of Hydraulic Research (IIHR), USA and the Instituto Nazionale per Studi ed Esperienze di Architettura Navale (INSEAN), Italy, with most of them for the zig-zag and turning circle maneuvers, and a few for the spiral and stopping maneuvers. Maneuvering in shallow water was also tested in the SIMMAN 2014. Experimental details can be found in the Tokyo 2015 computational fluid dynamics (CFD) Workshop in ship hydrodynamics and SIMMAN 2008, 2014, 2020.

Project supported by the National Natural Science Foundation of China (Grant Nos. 51979226, 52171324).
Biography: Peng Du (1989-), Male, Ph. D., Associate Professor, E-mail: dupeng@nwpu.edu.cn
Corresponding author: Hai-bao Hu
E-mail: huhaibao@nwpu.edu.cn

CFD simulations can accurately reproduce the experimental results. Because of the numerical complexity and the computational cost, the RANS-based CFD simulations becomes dominant choices[1-7]. Modeled propellers were sometimes used to lighten the computational burden[8], which is commonly-used in commercial codes (FINE-MARINE, STAR-CCM+, etc.).

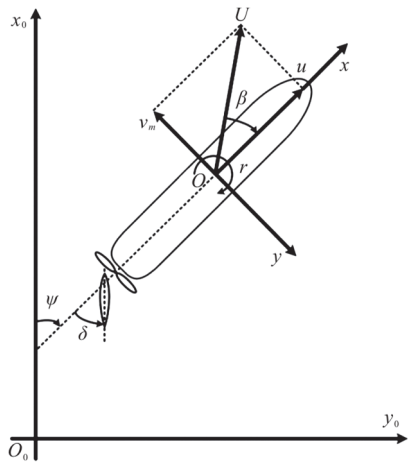

Fig. 1 Coordinate systems of the MMG model

Apart from the free running test, the mathematical modeling approach, also called the system-based method, is widely-used, where the calculation of the hydrodynamic coefficients is critical. This method is based on the rigid body equations:

$$X = m[\dot{u} - vr + wq - x_g(q^2 + r^2) + y_g(pq - \dot{r}) + z_g(pr + \dot{q})],$$

$$Y = m[\dot{v} - wp + ur - y_g(r^2 + p^2) + z_g(qr - \dot{p}) + x_g(qp + \dot{r})],$$

$$Z = m[\dot{w} - uq + vp - z_g(p^2 + q^2) + x_g(rp - \dot{q}) + y_g(rq + \dot{p})],$$

$$K = I_x\dot{p} + (I_z - I_y)qr - (\dot{r} + pq)I_{xz} + (r^2 - q^2)I_{yz} + (pr - \dot{q})I_{xy} + m[y_g(\dot{w} - uq + vp) - z_g(\dot{v} - wp + ur)],$$

$$M = I_y\dot{q} + (I_x - I_z)rp - (\dot{p} + qr)I_{xy} + (p^2 - r^2)I_{zx} + (qp - \dot{r})I_{yz} + m[z_g(\dot{u} - vr + wq) - x_g(\dot{w} - uq + vp)],$$

$$N = I_z\dot{r} + (I_y - I_x)pq - (\dot{q} + rp)I_{yz} + (q^2 - p^2)I_{xy} + (rq - \dot{p})I_{zx} + m[x_g(\dot{v} - wp + ur) - y_g(\dot{u} - vr + wq)] \quad (1)$$

where the first three equations are for the translational motions, while the last three for the rotational motions. The forces and the moments (X, Y, Z, K, M, N) on the right-hand side are expanded in Taylor series. (u, v, w, p, q, r) are the linear and angular velocities. $I_x, I_y, I_z, \cdots$ are the moments of inertia. (x_g, y_g, z_g) are the vector components from the gravity center to the rotation center. Their derivatives with respect to the variables (the velocity, the yaw rate, the rudder angle, etc.) give the hydrodynamic coefficients. Other forces generated by the wind, the waves, the current, the ship-ship interactions, etc. can also be included. Several models were proposed for calculating the hydrodynamic coefficients. The linearized models were used in early studies. Nonlinear models[9] become the trend currently. Among them, the Abkowitz model and the MMG model[9] are the most commonly-used. For the MMG model, the forces on the hull, the rudder, and the propeller are separated, and so are their hydrodynamic coefficients, while for the Abkowitz model, they are treated as a whole. The methods for determining the hydrodynamic coefficients include:

(1) The method of using the empirical formula is the most convenient but less accurate.

(2) The captive model test involves the forced ship motions obtained by using the planar motion mechanism (PMM) tests. Standard procedures were described in Refs. [10-11]. Experimental data can be found for the KVLCC1, the KVLCC2, the KCS, the DTMB 5415, and the ONRT in the Tokyo 2015 CFD Workshop in ship hydrodynamics and SIMMAN 2008, 2014, 2019[9, 12-14]. The CFD is used to simulate the experimental conditions numerically.

(3) The system identification can be used to calculate or correct the hydrodynamic coefficients based on the free running test results[12, 15-16]. To apply this method, the standard maneuvers should be conducted to obtain the system inputs (the rudder angle, the propeller revolution, etc.) and the outputs (the ship velocities, the heading, the yaw rate, etc.). The advantage of the system identification is that all the maneuvering coefficients can be estimated by one or a

few free running trials instead of numerous captive model tests. The classical system identification techniques for the ship maneuvering include the least squares method, the model reference method, the extended Kalman Filter method, the maximum likelihood method, the recursive prediction error method, and the annealing search method. However, some problems exist in these methods, such as the sensitivity to the initial values, the ill-conditioned solutions, the simultaneous drift of the parameters and the multicollinearity of the regressive parameters. Several new approaches were proposed for modeling the ship maneuvering, including the Markov process theories, the statistical linearization techniques, the frequency spectrum analysis, the optimization techniques, the genetic algorithm, the particle swarm optimization (PSO), the artificial neural networks (ANN), and the support vector machine (SVM). Among them, the ANN and the SVM can both be used in the parameter identification and the blind prediction of the ship maneuvering. For the parameter identification, the hydrodynamic coefficients can be obtained directly by the SVM whereas another regressor (e.g., the least squares method) is required by the ANN. For the blind prediction of the ship maneuvering, it is shown that SVM can be better generalized than the ANN. The sensitivity analysis can also be conducted to determine the most influential variables for the identification[17-19].

In this paper, the ship maneuvering analysis is carried out based on the virtual captive model tests. Commonly-used maneuvering models are analyzed, especially, the formulations and the procedures of the mathematical maneuvering group (MMG) model, based on the virtual captive model tests to obtain the hydrodynamic coefficients. The system-based maneuvering simulations are finally performed to calculate the trajectory, the heading angle, and other parameters of the vessel.

1. Maneuvering models

The system-based maneuvering simulations can be used to predict the ship trajectories, the yaw angles, and other parameters, which are important for the ship motion prediction and evaluation. As indicated by Eq. (1), the rigid body equations can be solved directly, where the hydrodynamic forces on the ship are calculated from the hydrodynamic derivatives obtained from either the empirical formula, the captive model tests or the system identification methods. Therefore, the hydrodynamic derivatives play an important role in the ship maneuvering simulations. A set of 3DOF rigid body equations is normally adopted for the simplification:

$$m(\dot{u}-vr-x_G r^2)=X(u,v,r,\dot{u},\dot{v},\dot{r},\delta,\cdots) \tag{2}$$

$$m(\dot{v}+ur+x_G\dot{r})=Y(u,v,r,\dot{u},\dot{v},\dot{r},\delta,\cdots) \tag{3}$$

$$I_z\dot{r}+mx_G(\dot{v}+ur)=N(u,v,r,\dot{u},\dot{v},\dot{r},\delta,\cdots) \tag{4}$$

The right-hand side can be expanded in the Taylor series as:

$$\begin{aligned}X=&X_0+(u-U)\frac{\partial X}{\partial u}+v\frac{\partial X}{\partial v}+r\frac{\partial X}{\partial r}+\dot{u}\frac{\partial X}{\partial \dot{u}}+\dot{v}\frac{\partial X}{\partial \dot{v}}+\\&\dot{r}\frac{\partial X}{\partial \dot{r}}+\delta\frac{\partial X}{\partial \delta}+\frac{1}{2!}\left[(u-U)\frac{\partial}{\partial u}+v\frac{\partial}{\partial v}+r\frac{\partial}{\partial r}+\right.\\&\left.\frac{\partial}{\partial \dot{u}}+\dot{v}\frac{\partial}{\partial \dot{v}}+\dot{r}\frac{\partial}{\partial \dot{r}}+\delta\frac{\partial}{\partial \delta}\right]^{-2}X+\cdots+\\&\frac{1}{n!}\left[(u-U)\frac{\partial}{\partial u}+v\frac{\partial}{\partial v}+r\frac{\partial}{\partial r}+\dot{u}\frac{\partial}{\partial \dot{u}}+\dot{v}\frac{\partial}{\partial \dot{v}}+\right.\\&\left.\dot{r}\frac{\partial}{\partial \dot{r}}+\delta\frac{\partial}{\partial \delta}\right]^{n}X+\cdots\end{aligned} \tag{5}$$

$$\begin{aligned}Y=&Y_0+(u-U)\frac{\partial Y}{\partial u}+v\frac{\partial Y}{\partial v}+r\frac{\partial Y}{\partial r}+\dot{u}\frac{\partial Y}{\partial \dot{u}}+\dot{v}\frac{\partial Y}{\partial \dot{v}}+\\&\dot{r}\frac{\partial Y}{\partial \dot{r}}+\delta\frac{\partial Y}{\partial \delta}+\frac{1}{2!}\left[(u-U)\frac{\partial}{\partial u}+v\frac{\partial}{\partial v}+r\frac{\partial}{\partial r}+\right.\\&\left.\frac{\partial}{\partial \dot{u}}+\dot{v}\frac{\partial}{\partial \dot{v}}+\dot{r}\frac{\partial}{\partial \dot{r}}+\delta\frac{\partial}{\partial \delta}\right]^{-2}Y+\cdots+\\&\frac{1}{n!}\left[(u-U)\frac{\partial}{\partial u}+v\frac{\partial}{\partial v}+r\frac{\partial}{\partial r}+\dot{u}\frac{\partial}{\partial \dot{u}}+\dot{v}\frac{\partial}{\partial \dot{v}}+\right.\\&\left.\dot{r}\frac{\partial}{\partial \dot{r}}+\delta\frac{\partial}{\partial \delta}\right]^{n}Y+\cdots\end{aligned} \tag{6}$$

$$\begin{aligned}N=&N_0+(u-U)\frac{\partial N}{\partial u}+v\frac{\partial N}{\partial v}+r\frac{\partial N}{\partial r}+\dot{u}\frac{\partial N}{\partial \dot{u}}+\dot{v}\frac{\partial N}{\partial \dot{v}}+\\&\dot{r}\frac{\partial N}{\partial \dot{r}}+\delta\frac{\partial N}{\partial \delta}+\frac{1}{2!}\left[(u-U)\frac{\partial}{\partial u}+v\frac{\partial}{\partial v}+r\frac{\partial}{\partial r}+\right.\\&\left.\frac{\partial}{\partial \dot{u}}+\dot{v}\frac{\partial}{\partial \dot{v}}+\dot{r}\frac{\partial}{\partial \dot{r}}+\delta\frac{\partial}{\partial \delta}\right]^{-2}N+\cdots+\\&\frac{1}{n!}\left[(u-U)\frac{\partial}{\partial u}+v\frac{\partial}{\partial v}+r\frac{\partial}{\partial r}+\dot{u}\frac{\partial}{\partial \dot{u}}+\dot{v}\frac{\partial}{\partial \dot{v}}+\right.\end{aligned}$$

$$\dot{r}\frac{\partial}{\partial \dot{r}}+\delta\frac{\partial}{\partial \delta}\Big]^{n} N+\cdots \tag{7}$$

The derivatives are usually expressed as:

$$\frac{\partial X}{\partial u}=X_u,\ \frac{\partial X}{\partial v}=X_v,\ \frac{\partial X}{\partial r}=X_r,\ \frac{\partial X}{\partial \dot{u}}=X_u,\cdots \tag{8}$$

Normally, only a few terms in Eqs. (5)-(7) are retained. In the early models, only the first order terms are kept, and they are referred as the linear models. Details of various models are discussed in the Introduction. Among them, the MMG[9] and Abkowitz models are the most commonly-used ones.

1.1 *Abkowitz model*

In the Abkowitz mathematical model, the forces and the moment X, Y and N in Eqs. (2)-(4) are directly expanded as:

$$\begin{aligned}X=&X_*+X_{\dot{u}}\dot{u}+X_u\Delta u+X_{uu}\Delta u^2+X_{uuu}\Delta u^3+X_{vv}v^2+\\&X_{vvu}v^2\Delta u+X_{rr}r^2+X_{rru}r^2\Delta u+X_{vr}vr+\\&X_{vru}vr\Delta u+X_{\delta\delta}\delta^2+X_{\delta\delta u}\delta^2\Delta u+X_{v\delta}v\delta+\\&X_{v\delta u}v\delta\Delta u+X_{r\delta}r\delta+X_{r\delta u}r\delta\Delta u\end{aligned} \tag{9}$$

$$\begin{aligned}Y=&Y_*+Y_{\dot{r}}\dot{r}+Y_{\dot{v}}\dot{v}+Y_u\Delta u+Y_{um}\Delta u^2+Y_{umu}\Delta u^3+Y_v v+\\&Y_{vv}v^3+Y_{vrr}vr^2+Y_{v\delta\delta}v\delta^2+Y_{vu}v\Delta u+Y_{vuu}v\Delta u^2+\\&Y_r r+Y_{rrr}r^3+Y_{vv}v^2r+Y_{r\delta\delta}r\delta^2+Y_{ru}r\Delta u+\\&Y_{ruu}r\Delta u^2+Y_\delta\delta+Y_{u\delta}\Delta u\delta+Y_{uu\delta}\delta\Delta u^2+\\&Y_{\delta\delta\delta}\delta^3+Y_{w\delta}v^2\delta+Y_{rr\delta}r^2\delta\end{aligned} \tag{10}$$

$$\begin{aligned}N=&N_*+N_{\dot{r}}\dot{r}+N_{\dot{v}}\dot{v}+N_u\Delta u+N_{uu}\Delta u^2+N_{uuu}\Delta u^3+\\&N_v v+N_{vvv}v^3+N_{vrr}vr^2+N_{v\delta\delta}v\delta^2+N_{vu}v\Delta u+\\&N_{vuu}v\Delta u^2+N_r r+N_{rrr}r^3+N_{vv}v^2r+N_{r\delta\delta}r\delta^2+\\&N_{ru}r\Delta u+N_{ruu}r\Delta u^2+N_\delta\delta+N_{u\delta}\Delta u\delta+\\&N_{uu\delta}\delta\Delta u^2+N_{\delta\delta\delta}\delta^3+N_{v\delta\delta}v^2\delta+N_{rr\delta}r^2\delta\end{aligned} \tag{11}$$

where Δu is the disturbance in the surge velocity, u_0 is the surge velocity in the initial state of the forward motion. Depending on the ship model and the maneuvering conditions, some terms can be neglected and the equations are thus simplified.

1.2 *MMG model*

The coordinate system of the MMG model is shown in Fig. 1. Similar to Eqs. (2)-(4), the set of 3DOF maneuvering equations of the MMG model with the added masses (m_x, m_y) and the added moment of inertia (J_z) is expressed as[9]:

$$X=(m+m_x)\dot{u}-(m+m_y)v_m r-x_G m r^2 \tag{12}$$

$$Y=(m+m_y)\dot{v}_m+(m+m_x)ur+x_G m\dot{r} \tag{13}$$

$$N_m=(I_{zG}+x_G^2 m+J_z)\dot{r}+x_G m(\dot{v}_m+ur) \tag{14}$$

On the other hand, the forces and the moments of the MMG model on the right-hand side are separated according to the hull, the propeller and the rudder:

$$X=X_H+X_R+X_P \tag{15}$$

$$Y=X_H+Y_R \tag{16}$$

$$N_m=N_H+N_R \tag{17}$$

This separation allows for more accurate and convenient evaluation of each force. Other forces induced by the wind, the waves, the current, the ship interactions, etc. can also be added in a similar way. It should be noted that this separation also brings errors due to the coupling effects, such as the hull-ruder-propeller interaction, the wave-current interaction, and the wave-wave interaction. Corrections can be considered in such situations. The hydrodynamic coefficients in the MMG model are deduced from the captive model tests.

1.2.1 Hydrodynamic forces on the hull

The hydrodynamic forces on the ship hull are non-dimensionalized as:

$$X_H=\frac{1}{2}\rho L_{pp}T_d U^2 X'_H(v'_m,r') \tag{18}$$

$$Y_H=\frac{1}{2}\rho L_{pp}T_d U^2 Y'_H(v'_m,r') \tag{19}$$

$$N_H=\frac{1}{2}\rho L_{pp}^2 T_d U^2 N'_H(v'_m,r') \tag{20}$$

where the dimensionless hydrodynamic forces are expressed in the 1st and 3rd order polynomial functions of v'_m and r':

$$X'_H(v'_m,r') = -R'_0 + X'_{vv}v'^2_m + X'_{vr}v'_m r' + X'_{rr}r'^2 + X'_{vvv}v'^4_m \tag{21}$$

$$Y'_H(v'_m,r') = Y'_v v'_m + Y'_R r' + Y'_{vvv}v'^3_m + Y'_{vvr}v'^2_m r' + Y'_{vr}v'_m r'^2 + Y'_{rrr}r'^3 \tag{22}$$

$$N'_H(v'_m,r') = N'_v v'_m + N'_R r' + N'_{vvv}v'^3_m + N'_{vvr}v'^2_m r' + N'_{vrr}v'_m r'^2 + N'_{rrr}r'^3 \tag{23}$$

The lateral velocity v_m, the yaw rate r are non-dimensionalized as $v'_m = v_m / U$, $r' = rL_{pp} / U$ respectively. Other forces and moments are non-domensionalized the same way as Eqs. (18)-(20). The non-dimensionalization is based on the Prime system II shown in Table 1.

Table 1 Standard normalization systems

Unit	Prime system I	Prime system II	Bis system
Length	L	L	L
Mass	$1/2\rho L^3$	$1/2\rho L^2 T_d$	$\mu\rho\nabla_S$
Inertia moment	$1/2\rho L^5$	$1/2\rho L^4 T_d$	$\mu\rho\nabla_S L^2$
Time	L/U	L/U	$\sqrt{L/g}$
Reference area	L^2	LT_d	$2\mu\nabla_S / L$
Position	L	L	L
Angle	1	1	1
Linear velocity	U	U	$\sqrt{Lg}$
Angular	U/L	U/L	$\sqrt{g/L}$
Linear	U^2/L	U^2/L	g
Angular	U^2/L^2	U^2/L^2	g/L
Force	$1/2\rho U^2 L^2$	$1/2\rho U^2 L T_d$	$\mu\rho g\nabla_S$
Moment	$1/2\rho U^2 L^3$	$1/2\rho U^2 L^2 T_d$	$\mu\rho g\nabla_S L$

1.2.2 Propeller induced forces

Only the longitudinal force induced by the propeller is considered

$$X_P = (1-t_P)T_P \tag{24}$$

where the thrust deduction factor t_P is assumed to be constant for a given propeller load for simplicity. The propeller thrust T_P is written as

$$T_P = \rho n_P^2 D_P^4 K_T(J_P) \tag{25}$$

$$K_T(J_P) = k_2 J_P^2 + k_1 J_P + k_0 \tag{26}$$

where k_0, k_1, k_2 are obtained from the propeller open water tests.

During the maneuvering simulations, the propeller advance ratio J_P is expressed as:

$$J_P = \frac{u(1-w_P)}{n_P D_P} \tag{27}$$

$$\frac{1-w_P}{1-w_{P0}} = 1 + [1-\exp(-C_1|\beta_P|)](C_2 - 1) \tag{28}$$

where w_P is the wake coefficient at the propeller position, w_{P0} is that in the straight moving state, β_p is the geometrical inflow angle to the propeller, β is the hull drift angle at the midship, x_P is the longitudinal coordinate of the propeller position and C_1, C_2 are the constants of the wake characteristics determined from experiments.

1.2.3 Rudder induced forces

The rudder induced forces are expressed as:

$$X_R = -(1-t_R)F_N \sin\delta \tag{29}$$

$$Y_R = -(1+a_H)F_N \cos\delta \tag{30}$$

$$N_R = -(x_R + a_H x_H)F_N \cos\delta \tag{31}$$

where t_R and a_H are the steering resistance deduction factor and the rudder force increase factor, x_R and x_H are the longitudinal coordinates of the rudder position and the acting point of the additional lateral force. They represent the interactions between the hull and the rudder.

The rudder normal force F_N is expressed as

$$F_N = \frac{1}{2}\rho A_R U_R^2 f_\alpha \sin\alpha_R \tag{32}$$

where ρ is the water density, A_R is the profile area of the rudder movable part and f_α is the rudder lift gradient coefficient. The rudder inflow velocity U_R and the angle α_R are expressed as:

$$U_R = \sqrt{u_R^2 + v_R^2} \tag{33}$$

$$\alpha_R \approx \delta - \frac{v_R}{u_R} \tag{34}$$

where δ is the rudder angle, u_R and v_R are the longitudinal and lateral inflow velocity components over the rudder:

$$u_R = \varepsilon_R u(1-w_P)\sqrt{\eta_R\left[1+\kappa_R\left(\sqrt{1+\frac{8K_T}{\pi J_P^2}}-1\right)\right]^2+(1+\eta_R)} \tag{35}$$

$$v_R = U\gamma_R\beta_R \tag{36}$$

where β_R is the effective inflow angle to the rudder, η_R is the ratio of the propeller diameter to the rudder span. ε_R is the wake fraction ratio at the rudder position to that at the propeller position and κ is an experimental constant.

2. Virtual captive model tests

A scaled model (L3) of the KVLCC2 tanker is selected in the captive model tests. The parameters of this ship are shown in Table 2. The virtual captive model tests are carried out under the propeller condition with the rudder. The ship speed U_0 is set to 0.76 m/s (15.5 kn in full-scale). Dimensionless variables are used in some cases and the Prime system II is adopted as the reference for their non-dimensionalizations (Table 1).

Table 2 Principal parameters of the KVLCC2 tanker

Parameter	L3 model	L7 model	Full-scale
Scale ratio, λ_s	1/110	1/45.7	1
Length between perpendiculars, L_{pp} /m	2.902	7	320
Ship breadth, B_{wl} /m	0.527	1.27	58
Ship draught, T_d /m	0.189	0.46	20.8
Displacement volume, V_s /m^3	0.235	3.27	312 600
Longitudinal gravity center position, x_G /m	0.102	0.25	11.2
Block coefficient, C_b	0.81	0.81	0.81
Propeller diameter, D_p /m	0.09	0.216	9.86
Rudder span length, H_R /m	0.144	0.345	15.8
Profile area of rudder movable part, A_R /m^2	0.00928	0.0539	112.5

2.1 *Hydrodynamic coefficients of the hull*

2.1.1 Actuator disk model for propeller

The oblique towing test (OTT) and circular motion test (CMT) will be carried out for the hull. Instead of a real propeller, an actuator disk model is implemented to account for the propulsion. The axial and tangential volume forces will be generated by the actuator disk to create a flow field similar to that created by a real propeller:

$$\boldsymbol{f}_{bx} = A_x r_d^* \sqrt{1-r_d^*}\,,\quad \boldsymbol{f}_{b\theta} = A_\theta \frac{r_d^*\sqrt{1-r_d^*}}{r_d^*(1-r_h')+r_h'} \tag{37}$$

where r_d is the radius of the disk, $r_d^* = (r_d' - r_h')/(1-r_h')$, $r_d' = r_d / R_P$. A_x and A_θ are expressed as:

$$A_x = \frac{105}{8}\frac{T_P}{\pi\Delta(3R_H+4R_P)(R_P-R_H)} \tag{38}$$

$$A_\theta = \frac{105}{8}\frac{Q_P}{\pi\Delta(R_P-R_H)(3R_P+4R_H)} \tag{39}$$

R_H, R_P are the radius range of the disk. The thrust T_P is obtained from the self-propulsion tests[9] and the torque Q_P can be calculated from the data of the open water test. When the ship moves, the position of the actuator disk should also be updated based on the two coordinate frames in Fig. 1:

$$x = (x_0 - x_{0G})\cos\psi + (y_0 - y_{0G})\sin\psi\,,$$

$$y = -(x_0 - x_{0G})\sin\psi + (y_0 - y_{0G})\cos\psi\,,\quad z = z_0 \tag{40}$$

It can be seen that the above equations are only updated in the horizontal plane as in the captive model tests without sinkage and trim.

2.1.2 Computational setups

The hydrodynamic derivatives of the hull are determined using the OTT, CMT. The planar motion mechanism (PMM) can also be used, but the obtained derivative values vary remarkably due to the influence of the motion frequency and the amplitude according to Ref. [9]. It should be noted that the simulations here are carried out without sinkage and trim. The open-source code OpenFOAM is used for the simulations in this work. The SST k-ω turbulence model is adopted. The time derivative terms are discretized using the implicit Euler scheme. The convec-

tion term in the momentum equation is discretized using the second order linear upwind scheme, and the convection term in the VOF equation is discretized using the second order total variation diminishing (TVD) scheme with van Leer's flux limiter. The second order central differencing scheme with non-orthogonal correction is used for the discretization of the diffusion term. Four outer correctors are used per time step, and three pressure corrections are employed in this case[20-24]. All equations are solved within the tolerance of $O(-8)$. More details are given in our earlier work[25]. The rudder angle $\delta = 0°$ in the tests.

(1) Oblique towing test

In the OTT, the hull drift angle β varies in the range of 0°-20° with an interval of 4°. The computational domain is designed as shown in Fig. 2. During the OTT simulations, the same mesh is used while the direction of the inlet velocities varies to realize different oblique conditions, to avoid remeshing at different ship drift angles. The actuator disk is located as the real propeller. The case setups are shown in Table 3. Five drift angles are designed in this study. The inlet velocity and the revolution rate of the KP458 propeller are 0.76 m/s, 17.95 rps. The thrust value is obtained from the experiment in Ref. [9]. The torque is obtained from the open water test according to the thrust.

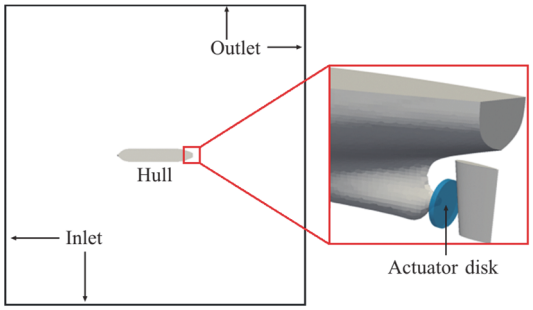

Fig. 2 (Color online) Computational domain and boundary conditions for the OTT, CMT

Table 3 Setups of the OTT, CMT

Parameters	Values
Ship drift angle, β /°	0, 4, 8, 12, 16, 20
Thrust, T /N	4.350, 4.321, 3.810, 4.054, 3.735, 3.784
Torque, Q /Nm	0.0884, 0.0872, 0.0822, 0.0845, 0.0815, 0.0820

(2) Circular motion test

In the CMT, the non-dimensional yaw rate r' varies in the range of 0-0.8 with an interval of 0.2 at a fixed drift angle. Figure 3 shows the typical movement in the CMT. The ship model is towed to move in a circular arc line. Since the yaw rate $r = U / R$, changing the turning radius R is equivalent to changing r at the same ship speed $U = 0.76\ \mathrm{m/s}$. The surge force, the lateral force and the yaw moment are measured during the tests. The thrust and the torque are determined the same way as the former part (Table 3). The position of the actuator disk is updated each time step according to Eq. (40).

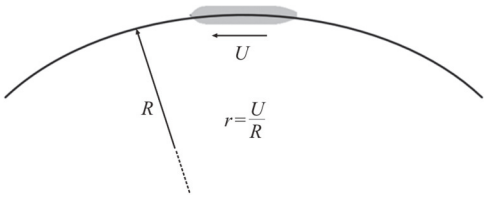

Fig. 3 Sketch of the CMT. r, R, U are the yaw rate, the turning radius and the ship speed

2.1.3 Results and analyses

(1) Oblique towing test

The validation and verification studies were carried out in our earlier work[25]. The feasibility of implementing the models is confirmed. The non-dimensional forces and moment are calculated as shown in Figs. 4-6. In the simulations, only positive drift angles are considered. The negative drift angle cases can be considered as the direct projections ed directly from the positive ones. The ship with larger drift angle has higher lateral force and yaw moment. The lateral force and the yaw moment in the OTT are in very good agreement with the experimental results[9]. For the longitudinal force, the values with negative drift angles are underestimated since they are projected directly from the positive ones.

(2) Circular motion test

The wave elevation generated by a ship of smaller drift angle is higher. The wave elevation is influenced by the volume force of the actuator disk. The velocity points to the inside of the turning circle in the CMT. The non-dimensionalized forces and moment are shown in Figs. 4-6.

(3) Hydrodynamic coefficient calculation

The coefficients of the actual measured force are expressed as:

$$X'_{mes} = X'^{*}_{H} + X'_{R} + X'_{P} \tag{41}$$

$$Y'_{mes} = Y'^{*}_{H} + Y'_{R} \tag{42}$$

$$Z'_{mes} = N'^{*}_{H} + N'_{R} \tag{43}$$

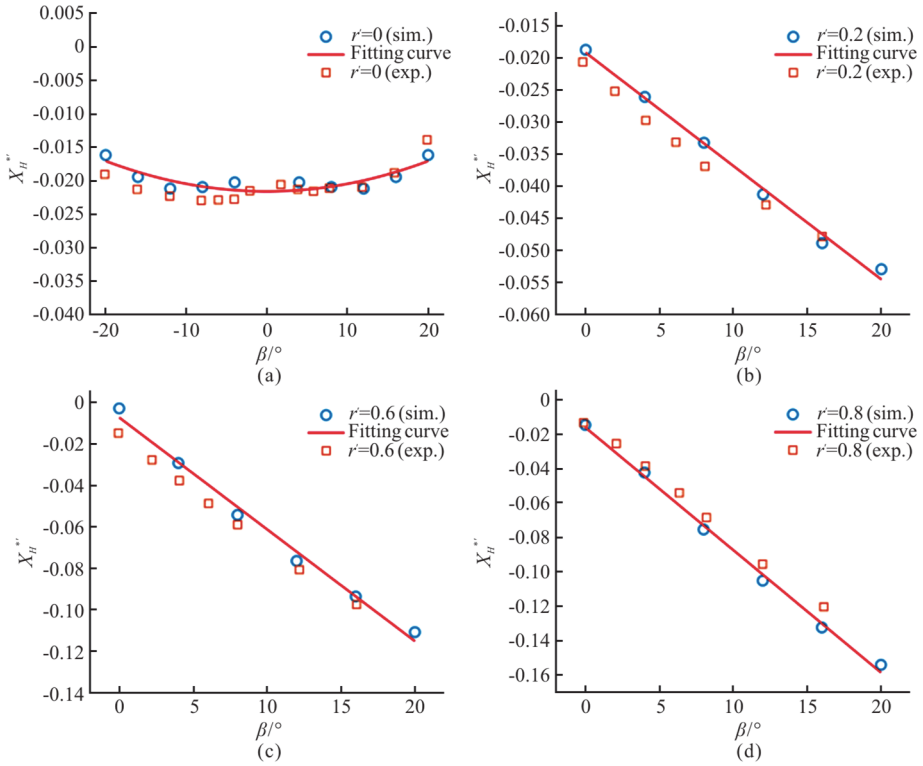

Fig. 4 (Color online) Non-dimensional surge force $(X_H^{*\prime})$ in OTT, CMT

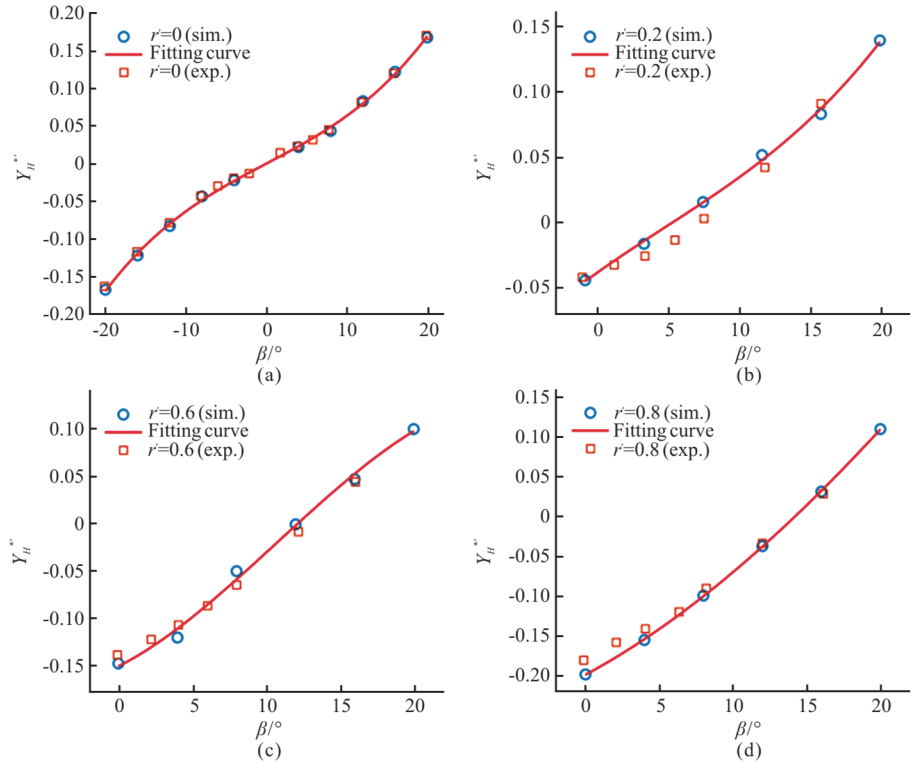

Fig. 5 (Color online) Non-dimensional lateral force $(Y_H^{*\prime})$ in OTT, CMT

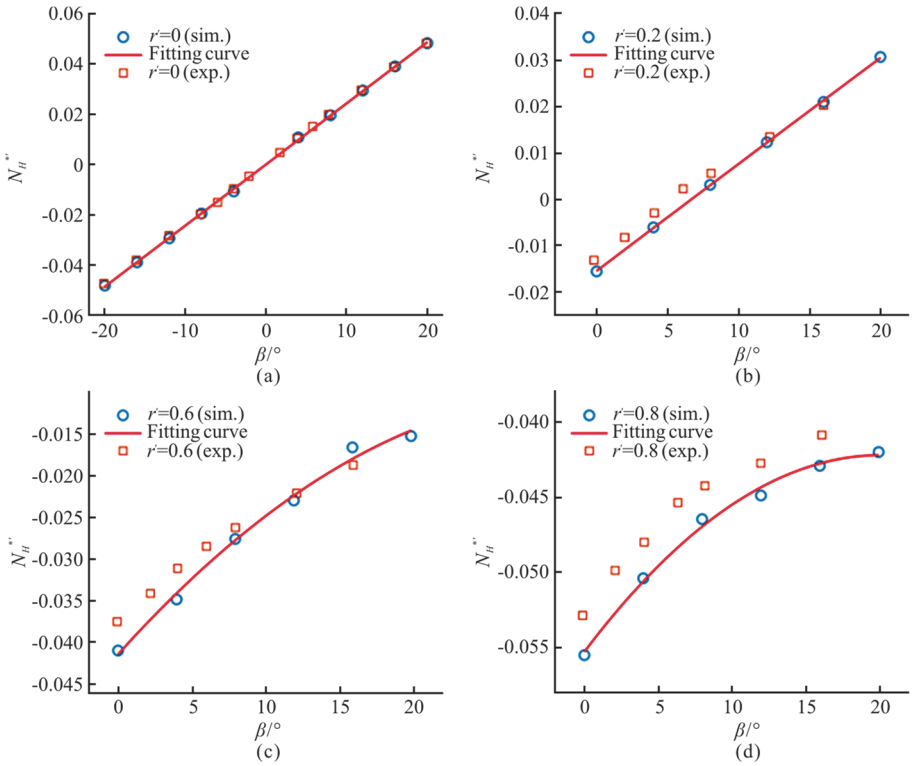

Fig. 6 (Color online) Non-dimensional yaw moment $(N_H^{*\prime})$ in OTT, CMT

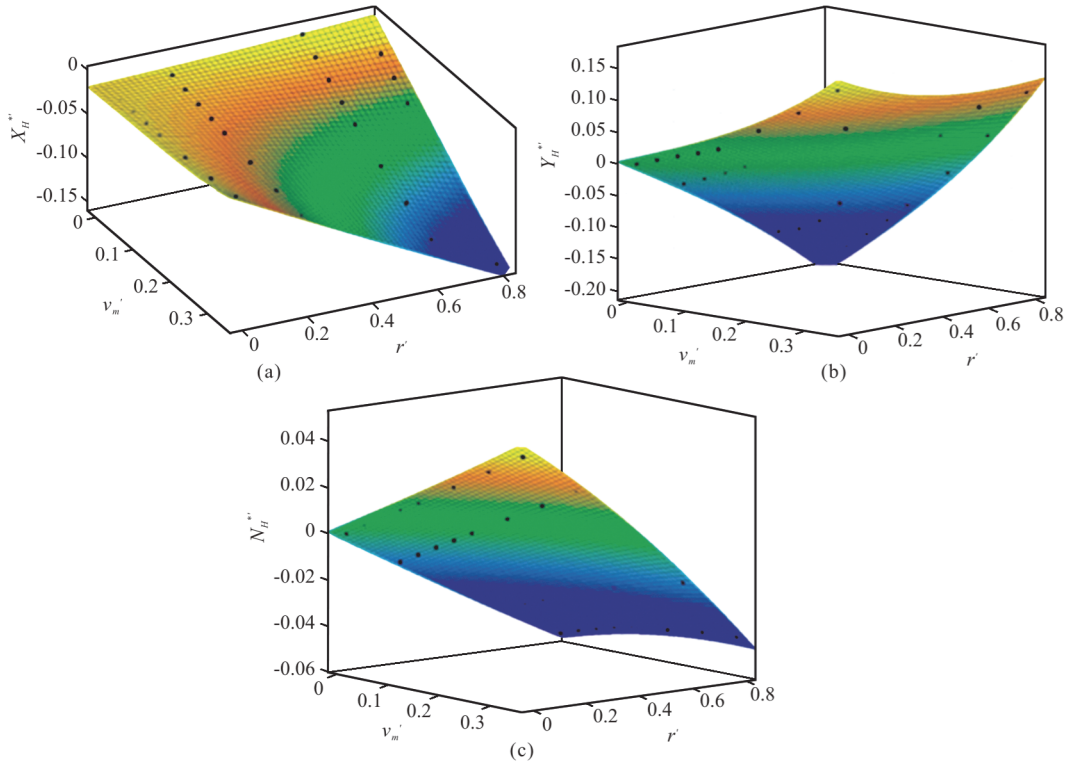

Fig. 7 (Color online) Fitting surfaces of the results of the OTT, CMT. v'_m, r' are the dimensionless lateral velocity and yaw rate. $X_H^{*\prime}$, $Y_H^{*\prime}$ and $N_H^{*\prime}$ are the dimensionless forces and moment on the hull

where

$$X'^{*}_{H} = X'_{H} + (m' + m'_{y})v'_{m}r' + x'_{G}m'r'^{2} \quad (44)$$

$$Y'^{*}_{H} = Y'_{H} - (m' + m'_{x})r' \quad (45)$$

$$N'^{*}_{H} = N'_{H} - x'_{G}m'r' \quad (46)$$

Here, an approximation of $u' \approx 1$ is employed. With $\delta = 0$, the following equations can be obtained:

$$X'^{*}_{H} = X'_{mes} - (1 - t_{p})T' \quad (47)$$

$$Y'^{*}_{H} = Y'_{mes} + (1 + a_{H})F'_{N} \quad (48)$$

$$Z'^{*}_{H} = N'_{mes} + (x'_{R} + a_{H}x'_{H})F'_{N} \quad (49)$$

X'^{*}_{H}, Y'^{*}_{H} and Z'^{*}_{H} can be calculated with X'_{mes}, Y'_{mes}, N'_{mes}, F'_{N} and T' being obtained from the CFD simulations. By substituting Eqs. (21)-(23) into Eqs. (44)-(46), the following expressions can be obtained for calculating the hydrodynamic derivatives:

$$X'^{*}_{H} = -R'_{0} + X'_{vv}v'^{2}_{m} + (X'_{vr} + m' + m'_{y})v'_{m}r' + (X'_{rr} + x'_{G}m')r'^{2} + X'_{vvvv}v'^{4}_{m} \quad (50)$$

$$Y'^{*}_{H} = Y'_{v}v'_{m} + (Y'_{R} - m' - m'_{x})r' + Y'_{vvv}v'^{3}_{m} + Y'_{vvr}v'^{2}_{m}r' + Y'_{vrr}v'_{m}r'^{2} + Y'_{rrr}r'^{3} \quad (51)$$

$$N'^{*}_{H} = N'_{v}v'_{m} + (N'_{R} - x'_{G}m')r' + N'_{vvv}v'^{3}_{m} + N'_{vvr}v'^{2}_{m}r' + N'_{vrr}v'_{m}r'^{2} + N'_{rrr}r'^{3} \quad (52)$$

The least squares method is adopted to fit these equations with the interpolated simulation results in Figs. 4-6. The fitting surfaces are shown in Fig. 7. The coefficient values can be found in Table 4, which agree with the experiment values except a few coefficients (X'_{rr}, Y'_{rrr} and N'_{rrr}). This is because the experiments covered a wider range comparably. In terms of $(X'_{vr} + m' + m'_{y})$, $(X'_{rr} + x'_{G}m')$ and $(N'_{R} - x'_{G}m')$, the added mass components are calculated as follows:

(1) m' is given from the displacement volume of the ship.

(2) m'_{x}, m'_{y} and J'_{z} are estimated by the Motora's empirical chart.

The final hydrodynamic derivatives and added masses of the hull are shown in Table 4.

Table 4 Hydrodynamic derivatives and added masses of the hull

Coefficient	Exp.	Sim.
R'_{0}	0.022	0.019
X'_{vv}	–0.040	–0.061
$X'_{vr} + m' + m'_{y}$	0.518	0.525
X'_{vr}	0.002	0.007
$X'_{rr} + x'_{G}m'$	0.021	0.009
X'_{rr}	0.011	-0.001
X'_{vvvv}	0.771	0.730
Y'_{v}	–0.315	–0.355
$Y'_{R} - m' - m'_{x}$	–0.233	–0.218
Y'_{R}	0.083	0.084
Y'_{vvvv}	–1.607	–1.161
Y'_{vvr}	0.379	0.288
Y'_{vrr}	–0.391	–0.548
Y'_{rrr}	0.008	0.059
N'_{v}	–0.137	–0.139
$N'_{R} - x'_{G}m'$	–0.059	–0.070
N'_{R}	–0.049	–0.060
N'_{vvv}	–0.030	–0.027
N'_{vvr}	–0.294	–0.143
N'_{vrr}	0.055	0.099
N'_{rrr}	–0.013	–0.002
m'_{x}	0.022	-
m'_{y}	0.223	-
J'_{z}	0.011	-

2.2 *Rudder force tests*

2.2.1 Computational setups

The rudder force tests are conducted in a straight moving state with a fixed rudder angle (0°-20° with an interval of 5° in the tests, $\beta = 0$, $r' = 0$). Since the flow details are important for predicting the loads on the propeller, a real propeller is modeled in these tests. The propeller revolution n_{P} is 17.95 rps. The non-dimensional forms of Eqs. (15)-(17) can then be simplified as:

$$X' = -R'_{0} + (1 - t_{P})T' - (1 - t_{R})F'_{N}\sin\delta \quad (53)$$

$$Y' = -(1 + a_{H})F'_{N}\cos\delta \quad (54)$$

$$N'_{m} = -(x'_{R} + a_{H}x'_{H})F'_{N}\cos\delta \quad (55)$$

The computational meshes are shown in Fig. 8. The arbitrary mesh interface (AMI) technique is used for the propeller rotation. The rudder, the propeller and its downwind are refined to capture the flow characteristics.

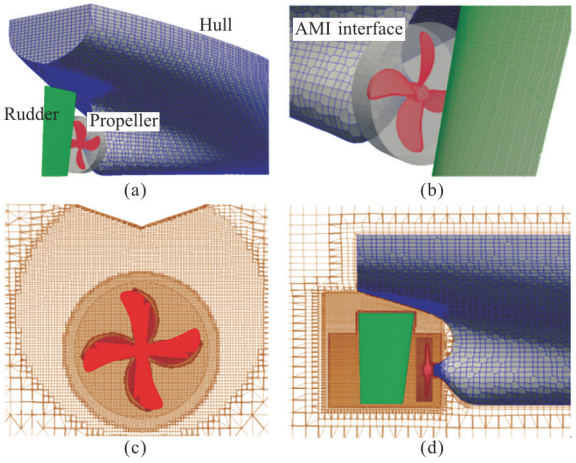

Fig. 8 (Color online) Computational domain and mesh for the rudder force tests. (a) The positions of the hull, the rudder and the propeller, (b) Zooms of the AMI position, (c) and (d) The mesh refinements at two cross sections of the propeller

2.2.2 Results and analyses

The flows at the propeller position will be accelerated by the propeller and directed by the rudder, which is also the mechanism of the advancing and the turning of the ship. In Fig. 9, the longitudinal force, the lateral force, the yaw moment and the rudder normal force are calculated and compared with experiments[9]. Except the longitudinal force, others are approximately linear with respect to the rudder angle. The propeller thrust remains the same at different rudder angles. Based on Eqs. (53)-(55), the relations between the forces and the moment on the hull and the rudder forces are shown in Fig. 10. The hydrodynamic coefficients t_R, a_H and x'_H can then be obtained from the slopes. The calculated rudder coefficients are shown in Table 5. Deviations can be clearly observed since only five cases are simulated in our work. More simulations can be done to reduce the computational and fitting errors.

Other coefficients of the rudder are determined as follows:

(1) The longitudinal coordinate of the rudder position x_R is approximately $-0.5L_{pp}$, i.e., $x'_P = -0.5$.

(2) Rudder lift gradient coefficient $f_\alpha = 6.13\Lambda/(\Lambda+2.25)$ is estimated using the formula with a practical treatment for the mariner rudder by[9]. $\Lambda = B_R / C_R$ is the aspect ratio of the rudder including the horn part, where B_R and C_R are the rudder span and the chord length, respectively.

(3) κ and ε are determined from the rudder force test results in a straight moving state under various propeller loads. Their values are directly taken from Ref. [9].

(4) γ_R and l'_R are calculated by fitting the data from the OTT and the flow straightening coefficient tests, which are taken from Ref. [9].

2.3 *Open water tests of the propeller*

2.3.1 Computational setups

The open water test is used to determine the hydrodynamic coefficients k_0, k_1 and k_2 for the propeller. The KP458 propeller is adopted with the KVLCC2 model, whose geometrical parameters are shown in Fig. 11. The computational domain is designed as 5 propeller diameters (D_P) upstream, 10 diameters downstream and 10 diameters in the lateral direction. The grid of the propeller is refined gradually and the grids of the edges of the blades are further refined with a higher level grid to capture the tip vortices. The grid number and the time step are 1 089 926 and 10^{-3} s, respectively. The whole domain rotates with a prescribed rotation velocity. The inlet velocity (U_{in}) is varied to obtain different advance coefficients $(J_P = U_{\text{in}} / n_p D_p)$.

2.3.2 Results and analyses

The single run approach, with the inlet velocity being increased with a small acceleration, is adopted instead of the multi-run approach to reduce the computational time.

In the single run method, the acceleration should be small enough to make the time derivative negligible, thus the solution process is in a quasi-steady state. The result is shown in Fig. 12, which covers a wide range in a single run. Overally, the simulation result agrees with the experiments. However, since the initial values may be not realistic, it will take time for the flows to reach a balanced state.

The values of k_0, k_1 and k_2 are calculated according to Eq. (26) and shown in Table 6. They are captured accurately by the single-run approach. The thrust (T_P) and the torque (Q_P) for the actuator disk model can be calculated according to the simulation results:

$$K_T = \frac{T_P}{\rho n_P^2 D_P^4}, \quad K_Q = \frac{Q_P}{\rho n_P^2 D_P^5} \tag{56}$$

The determination procedures of other propeller coefficients are as follows:

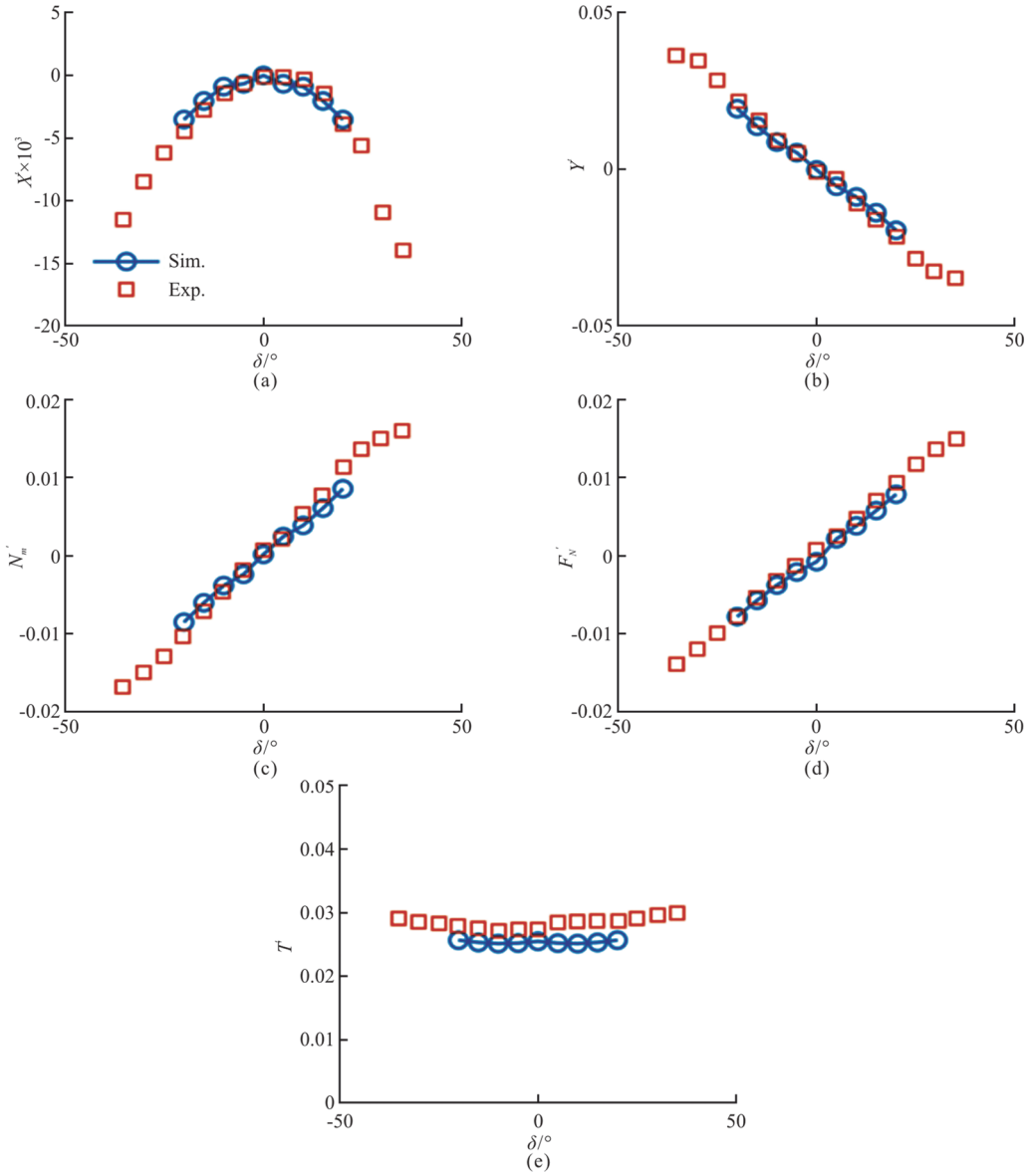

Fig. 9 (Color online) Simulation results of the rudder force tests. X', Y', N'_m, F'_N and δ are the dimensionless longitudinal force, lateral force, yaw moment around midship, rudder normal force, propeller thrust and rudder angle, respectively

(1) The thrust deduction factor t_P is calculated according to Eq. (53). The R'_0 value is already obtained. The torque (T') can be obtained from Fig. 12. It can be seen that it is not affected by the rudder angle. The thrust deduction coefficient value is shown in Table 6.

(2) The wake characteristic constants C_1, C_1 are taken from Ref. [9] directly.

(3) The longitudinal coordinate of the propeller position x_P is approximately $-0.5L_{pp}$, i.e., $x'_P = -0.5$.

(4) Effective wake in the straight moving state w_{P0} is assumed to be 0.40 for the L7-model and 0.35 for the full-scale as in Ref. [9].

3. Maneuvering simulations

Using the hydrodynamic coefficients obtained in Tables 4, 5 and 6, the maneuvering simulations are performed for the KVLCC2 L7 model (Table 2). The initial velocity U_0 is 0.76 m/s. The propeller revolution is assumed to keep a constant U_0. The turning circle tests $(\delta = \pm 35°)$ and the zigzag tests $(\delta = \pm 10°/\pm 20°)$ are simulated using the MMG model described in Section 1.2. The free running model tests

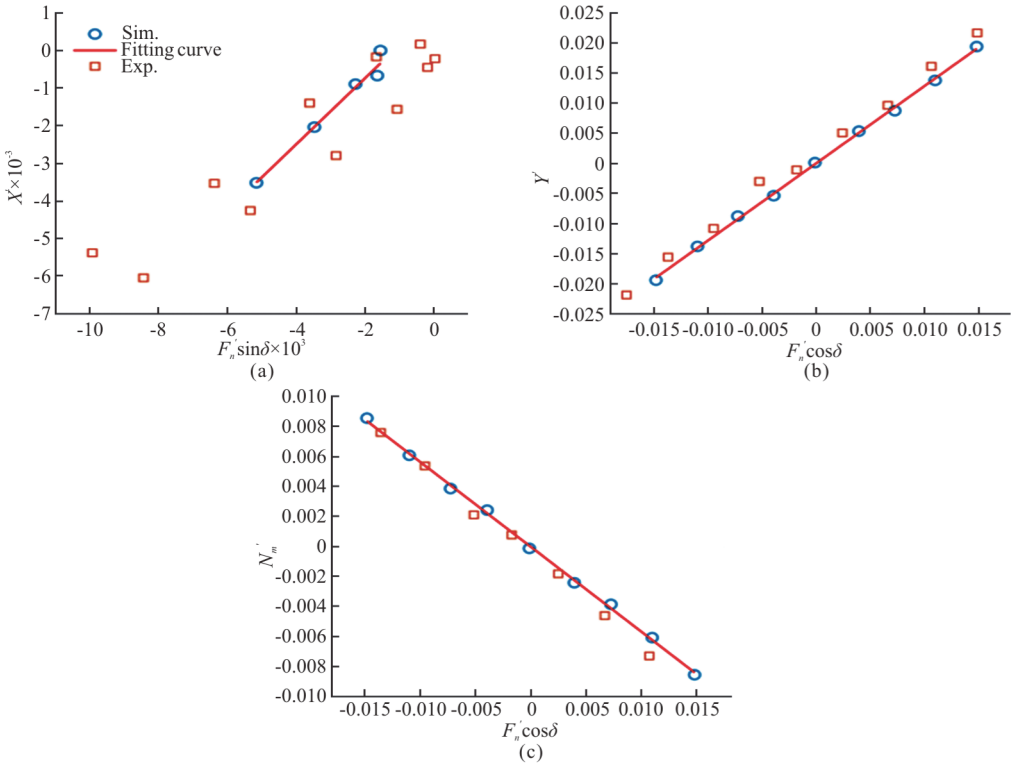

Fig. 10 (Color online) Analysis results of the rudder force tests. X', Y', N_m', F_N' and δ are the dimensionless longitudinal force, lateral force, yaw moment around midship, rudder normal force and rudder angle, respectively

Table 5 Hydrodynamic coefficients obtained from the rudder force tests

Coefficients	Exp.	Sim.
t_R	0.387	0.123
a_H	0.312	0.284
x_H'	0.312	0.284
f_α	2.747	-
x_R'	–0.5	-
κ	0.5	-
ε	1.09	-
$\gamma_R(\beta_R<0)$	0.395	-
$\gamma_R(\beta_R>0)$	0.640	-
l_R'	–0.71	-

were carried out in the Maritime Research Institute Netherlands (MARIN) and are used for comparison here (Figs. 13-18).

The turning circle tests are normally conducted with two directions, with positive and negative rudder angles (Figs. 13, 14), to test the turning ability in both directions. From the dimensionless trajectory, the absolute velocity $(U=\sqrt{u^2+v^2})$, the heading angle (ψ) and the yaw rate (r), it can be clearly seen that the ship velocity and the heading angle are predicted accurately. The largest error of the ship velocity is 7.6%, while that of the heading angle is 4.3%. However, the yaw rate is relatively harder to predict. Although the trends of the experiment and the simulations are similar. The maximum value is clearly underestimated by the simulation, with the largest error reaching 16.8%. This underestimation causes the deviation of the ship trajectory. The predicted turning radius is also smaller.

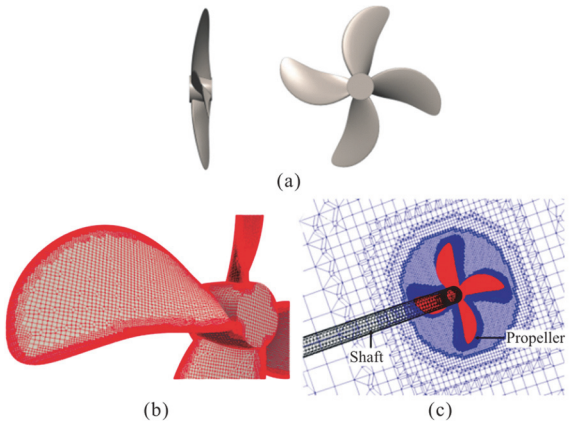

Fig. 11 (Color online) (a) Geometry of the propeller, (b) Local refinement of the mesh of the blade, (c) Gradual mesh refinement at the propeller position (Propeller information: (1) Diameter (0.09 m), (2) Pitch ratio (0.721), (3) Area ratio (0.431), Hub ratio (0.155))

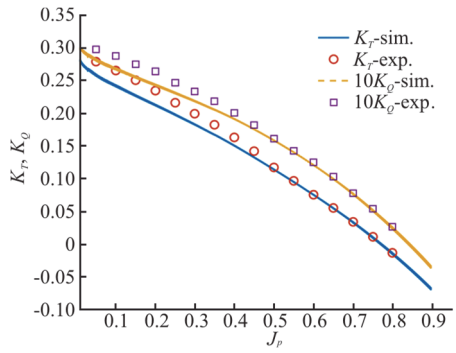

Fig. 12 (Color online) Open water test results for the KP458 propeller (K_T , K_Q are the thrust and torque coefficients, J_P is the advance ratio)

The zigzag tests are more difficult to perform since the rudder angle changes constantly (Figs. 15-18). Two directions are also tested for comparison. Good agreement between experiments and simulations can be observed at the beginning. However, the error accumulates and grows to a higher level, leading to the underestimation of all the parameters. The largest error of the absolute velocity $(U=\sqrt{u^2+v^2})$, the heading angle (ψ) and the yaw rate (r) are 5.5%, 21.2% and 16.3%, respectively. Since the experiments are only for a short time, the accuracy of the results are hard to evaluate for a long time range. It is certain that the deviation grows with the error accumulation.

Generally, the maneuvering simulations can correctly predict the ship motion with an acceptable accuracy, which shows the validity of the procedure in this work.

4. Conclusions and discussions

The maneuvering analysis is carried out based on the MMG model in this work, where the forces on the hull, the rudder and the propeller are separated. The MMG model is implemented in the virtual tank by using CFD techniques.

The whole virtual captive model tests are carried out using a L3 KVLCC2 model. The actuator disk model replaces the real propeller, to reduce the computational cost and to simplify the numerical treatment. The open water test, the rudder force test, the OTT, CMT are carried out to measure the forces and the moment on the propeller, the rudder and the hull. And the hydrodynamic derivatives are calculated mathematically. By designing the tests, the number of cases is reduced to a low level, which allows us to evaluate the maneuverability with a low cost and in a short time.

Based on the obtained hydrodynamic coefficients, the system-based maneuvering simulations, including the turning circle and zig-zag maneuvers, are conducted and the results are compared with those of the free running test. The good agreement shows the validity and the accuracy of the proposed model and procedure.

The CFD is a good alternative for the experimental approach. With the current advances, the CFD is able to predict the ship motions with a fairly good accuracy. In the current work, some simplifications are made to improve the efficiency of CFD without affecting the accuracy. However, it is still far from enough as far as the engineering purposes are concerned. New algorithms of the CFD and the computer technology should be developed to realize this purpose.

Acknowledgements

This work was supported by the Guangdong Basic and Applied Basic Research Foundation (Grant No. 2019A1515110863), the Fundamental Research Funds for the Central Universities (Grant No. 3102020HHZY030004), the Natural Science Basic Research Program of Shanxi (Grant No. 2020JC-18) and the Shanxi Provincial Key Research and Development Program (Grant No. 2021KW-38).

Table 6 Hydrodynamic coefficients of the propeller

Coefficients	Exp.	Sim.	Multi-run (sim.)	Single-run (sim.)	Value
k_0	0.2931	-	0.2754	0.2720	-
k_1	–0.2753	-	–0.2595	–0.2513	-
k_2	–0.1385	-	–0.1334	–0.1347	-
t_p	0.220	0.209	-	-	-
C_1	-	-	-	-	2.0
$C_2(\beta_p<0)$	-	-	-	-	1.1
$C_2(\beta_p>0)$	-	-	-	-	1.6
x'_p	-	-	-	-	–0.5
w_{p0} (L7 model)	-	-	-	-	–0.50
w_{p0} (full-scale)	-	-	-	-	0.35

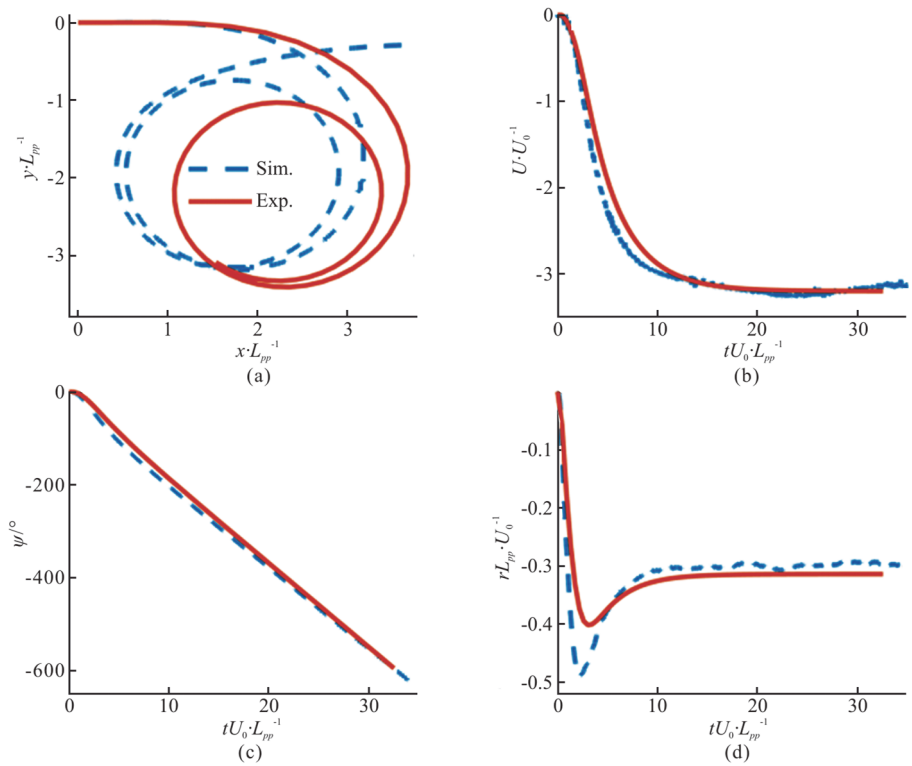

Fig. 13 (Color online) Turning circle maneuver ($\delta = 35°$) of the KVLCC2 L7 model. U, ψ, r, L_{pp} are the absolute velocity, the heading angle, the yaw rate and the ship length, respectively

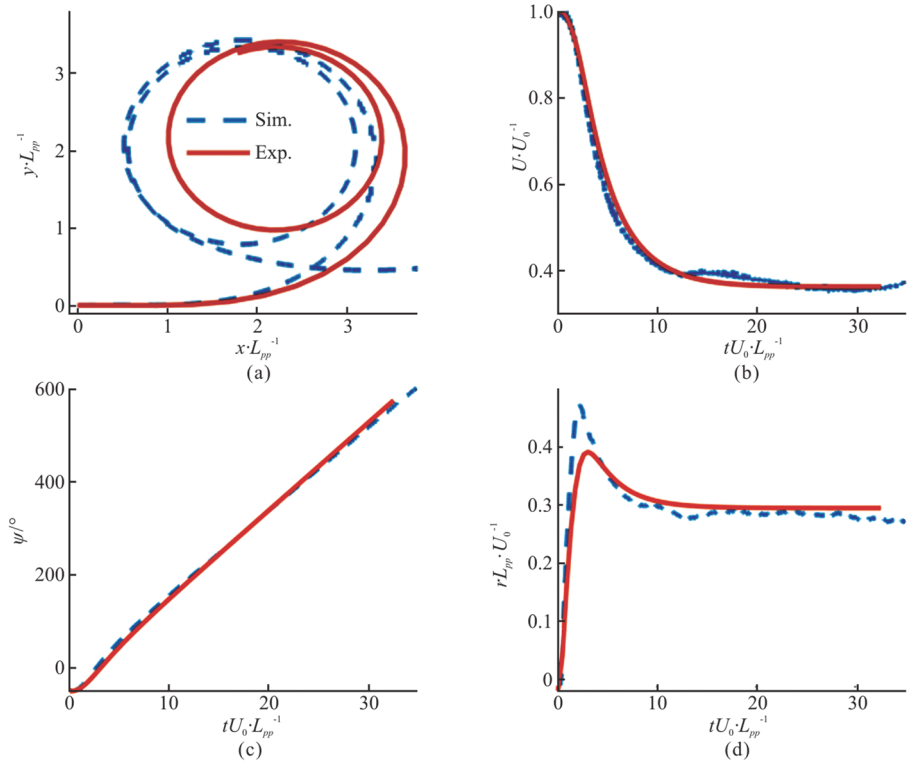

Fig. 14 (Color online) Turning circle maneuver ($\delta = -35°$) of the KVLCC2 L7 model. U, ψ, r, L_{pp} are the absolute velocity, the heading angle, the yaw rate and the ship length, respectively

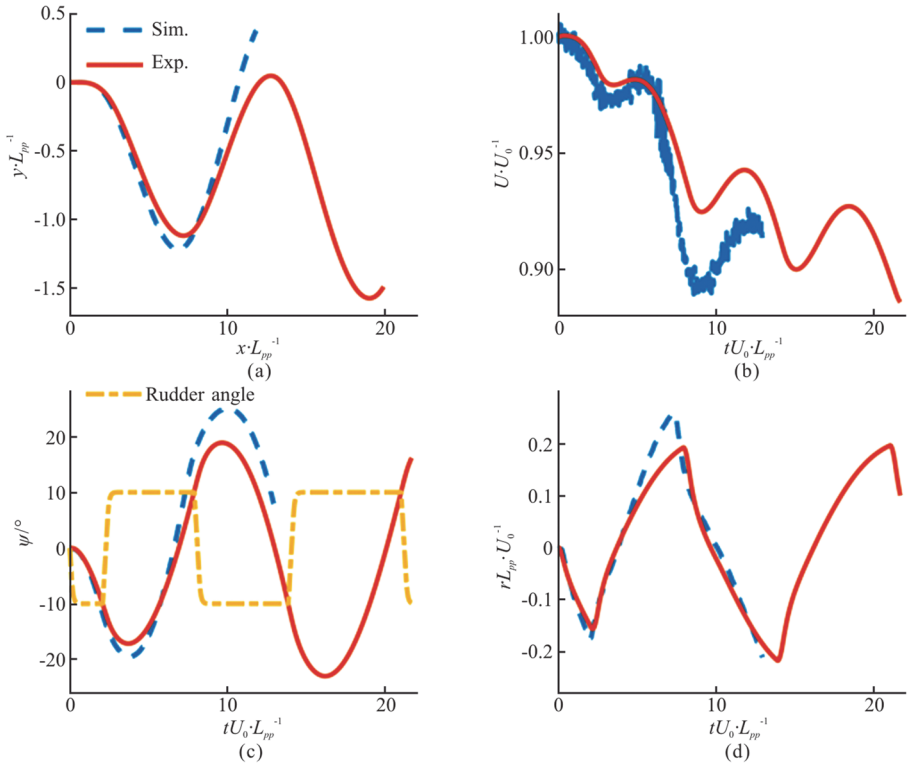

Fig. 15 (Color online) Zigzag maneuver ($\delta = 10°/-10°$) of the KVLCC2 L7 model. U, ψ, r, L_{pp} are the absolute velocity, the heading angle, the yaw rate and the ship length, respectively

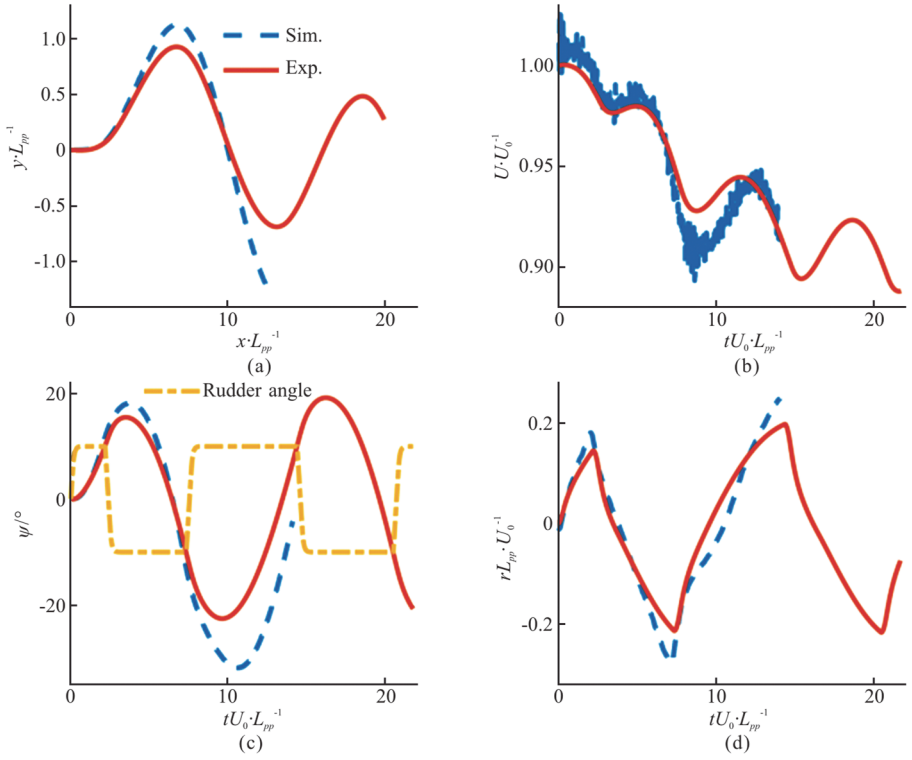

Fig. 16 (Color online) Zigzag maneuver ($\delta = -10°/10°$) of the KVLCC2 L7 model. U, ψ, r, L_{pp} are the absolute velocity, the heading angle, the yaw rate and the ship length, respectively

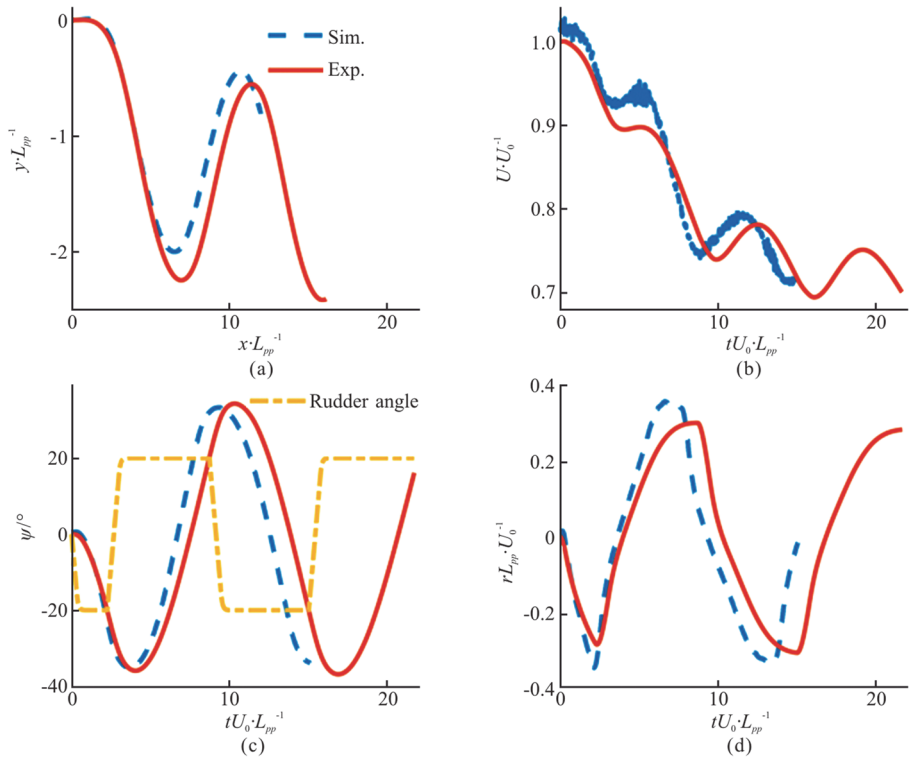

Fig. 17 (Color online) Zigzag maneuver ($\delta = 20°/-20°$) of the KVLCC2 L7 model. U, ψ, r, L_{pp} are the absolute velocity, the heading angle, the yaw rate and the ship length, respectively

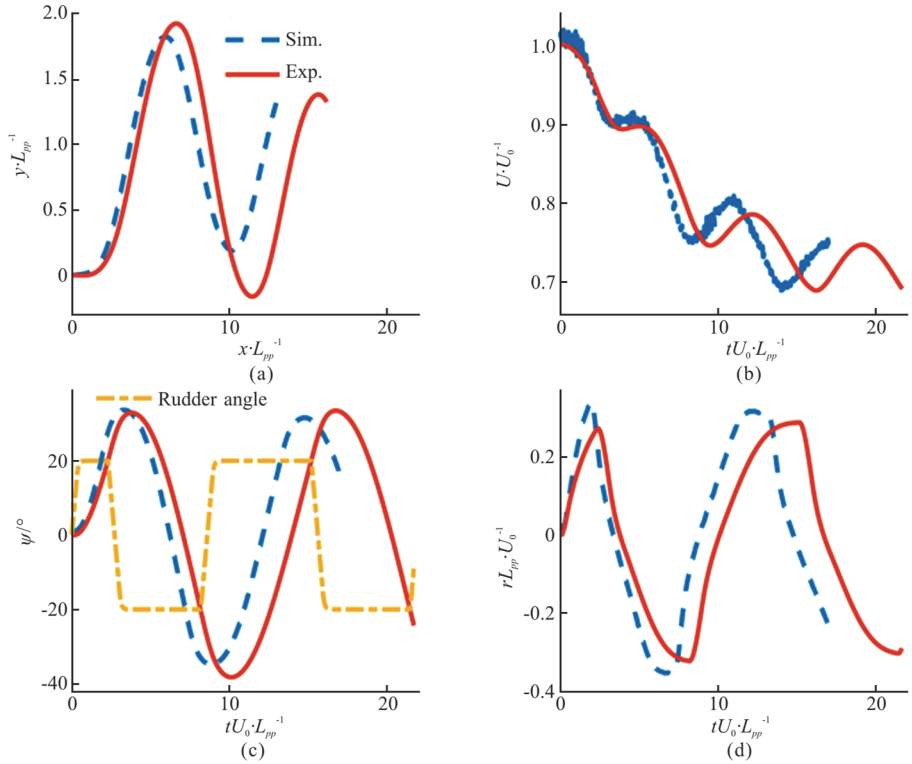

Fig. 18 (Color online) Zigzag maneuver ($\delta = -20°/20°$) of the KVLCC2 L7 model. U, ψ, r, L_{pp} are the absolute velocity, the heading angle, the yaw rate and the ship length, respectively

References

[1] Carrica P. M., Mofidi A., Eloot K. et al. Direct simulation and experimental study of zigzag maneuver of kcs in shallow water [J]. *Ocean engineering*, 2016, 112: 117-133.

[2] Mofidi A., Carrica P. M. Simulations of zigzag maneuvers for a container ship with direct moving rudder and propeller [J]. *Computers and Fluids*, 2014, 96: 191-203.

[3] Dubbioso G., Muscari R., Ortolani F. et al. Analysis of propeller bearing loads by CFD. Part I: Straight ahead and steady turning maneuvers [J]. *Ocean Engineering*, 2017, 130: 241-259.

[4] Broglia R., Dubbioso G., Durante D. et al. Turning ability analysis of a fully appended twin screw vessel by CFD. Part I: Single rudder configuration [J]. *Ocean engineering*, 2015, 105: 275-286.

[5] Wang J., Zou L., Wan D. Numerical simulations of zigzag maneuver of free running ship in waves by rans-overset grid method [J]. *Ocean Engineering*, 2018, 162: 55-79.

[6] Shen Z., Wan D., Carrica P. M. Dynamic overset grids in openfoam with application to kcs self-propulsion and maneuvering [J]. *Ocean Engineering*, 2015, 108: 287-306.

[7] Wang J., Wan D. CFD study of ship stopping maneuver by overset grid technique [J]. *Ocean Engineering*, 2020, 197: 106895.

[8] Carrica P. M., Ismail F., Hyman M. et al. Turn and zigzag maneuvers of a surface combatant using a urans approach with dynamic overset grids [J]. *Journal of Marine Science and Technology*, 2013, 18(2): 166-181.

[9] Yasukawa H., Yoshimura Y. Introduction of MMG standard method for ship maneuvering predictions [J]. *Journal of Marine Science and Technology*, 2015, 20(1): 37-52.

[10] ITTC. Recommended procedures and guidelines: Captive model test [C]. *Manoeuvring Committee of the 28th ITTC*, Wuxi, China, 2017.

[11] ITTC. Recommended procedures and guidelines: Captive model test procedure [C]. *Manoeuvring Committee of the 27th ITTC*, Copenhagen, Denmark, 2014.

[12] Stern F., Agdrup K., Kim S. Y. et al. Experience from simman 2008–The first workshop on verification and validation of ship maneuvering simulation methods [J]. *Journal of Ship Research*, 2011, 55(2): 135-147.

[13] Simonsen C. D., Otzen J. F., Klimt C. et al. Maneuvering predictions in the early design phase using cfd generated pmm data [C]. *29th Symposium on Naval Hydrodynamics*, Gothenburg, Sweden, 2012, 26-31.

[14] Sakamoto N., Carrica P. M., Stern F. Urans simulations of static and dynamic maneuvering for surface combatant: Part 1. verification and validation for forces, moment, and hydrodynamic derivatives [J]. *Journal of Marine Science and Technology*, 2012, 17(4): 422-445.

[15] Luo W., Soares C. G., Zou Z. Parameter identification of ship maneuvering model based on support vector machines and particle swarm optimization [J]. *Journal of Offshore Mechanics and Arctic Engineering*, 2016, 138(3): 031101.

[16] Sutulo S., Soares C. G. An algorithm for offline identification of ship manoeuvring mathematical models from free-running tests [J]. *Ocean Engineering*, 2014, 79: 10-25.

[17] Wang X., Zou Z., Xu F. et al. Sensitivity analysis and parametric identification for ship manoeuvring in 4 degrees of freedom [J]. *Journal of Marine Science and Technology*, 2014, 19(4): 394-405.

[18] Khanh T. T., Ouahsine A., Naceur H. et al. Assessment of ship manoeuvrability by using a coupling between a nonlinear transient manoeuvring model and mathematical programming techniques [J]. *Journal of Hydrodynamics*, 2013, 25(5): 788-804.

[19] Du P., Ouahsine A., Toan K. T. et al. Simulation of ship maneuvering in a confined waterway using a nonlinear model based on optimization techniques [J]. *Ocean Engineering*, 2017, 142: 194-203.

[20] Zhang X., Wang J., Wan D. Euler–lagrange study of bubble drag reduction in turbulent channel flow and boundary layer flow [J]. *Physics of Fluids*, 2020, 32(2): 027101.

[21] Zhang X. S., Wang J. H., Wan D. C. Numerical techniques for coupling hydrodynamic problems in ship and ocean engineering [J]. *Journal of Hydrodynamics*, 2020, 32(2): 212-233.

[22] Wang S. P., Zhang A. M., Liu Y. L. et al. Bubble dynamics and its applications [J]. *Journal of Hydrodynamics*, 2018, 30(6): 975-991.

[23] Xie Z., Zhang Y., Zhou J. et al. Theoretical and experimental research on the micro interface lubrication regime of water lubricated bearing [J]. *Mechanical Systems and Signal Processing*, 2021, 151: 107422.

[24] Wang J., Li H., Guo W. et al. Rayleigh–Taylor instability of cylindrical water droplet induced by laser-produced cavitation bubble [J]. *Journal of Fluid Mechanics*, 2021, 919: A42.

[25] Du P., Ouahsine A., Hoarau Y. Solid body motion prediction using a unit quaternion-based solver with actuator disk [J]. *Comptes Rendus Mécanique*, 2018, 346(12): 1136-1152.